南京航空航天大学

论 文 集

（二〇〇九年） 第47册

其 他

（第1分册）

南京航空航天大学科技部编

二〇一〇年五月

Z427/1033(2009)-(47)

NUAA2010055245

Z427
1033(2009)-(47)

其　他

南京航空航天大学
藏书
图书馆

2010055245

(47)

目录 1

序号	姓名	职称	单位	论文题目	刊物、会议名称	年、卷、期
1	余永辉	副教授	航天学院	A numerical model characterizing internal gravity wave propagation into the upper atmosphere	Advances in Space Research	2009 年，44 卷，7 期
2	井庆丰	讲师	航天学院	Adaptive compensating method for Doppler frequency shift using LMS and phase estimation	JOURNAL OF SYSTEMS ENGINEERING AND ELECTRONICS	2009 年 20 卷 5 期
3	刘燕斌	讲师	航天学院	高超声速飞行器建模与控制的一体化设计	宇航学报	2009 年 30 卷 6 期
4	刘燕斌	讲师	航天学院	Nonlinear fuzzy robust adaptive control of a longitudinal hypersonic aircraft model	Proceedings of the 2009 International Conference on Artificial Intelligence and Computational Intelligence	7-8 Novembe r,2009
5	刘燕斌	讲师	航天学院	Nonlinear adaptive inversion control with neural network compensation for a longitudinal hypersonic vehicle model	Proceedings of 2009 IEEE International Conference on Intelligent Computing and Intelligent Systems	22-23 Novembe r,2009
6	刘燕斌	讲师	航天学院	基于教育心理学理论的高等教育教学策略的研究	文教资料	2009 年 6 期
7	闫钧华	副教授	航天信息与应用系	Multi agent 在分布式测控系统动态任务调度中的实现	计算机工程与应用	20 09 年 45 卷 2 期
8	于佳 宗鹏	研究生，教授	航天学院	The simulation of lunar exploration and image transmission	Proceedings of the 2nd International Conference on Advanced Computer Theory and Engineering	213-220 Sep.25-27 2009
9	徐诚 宗鹏	研究生，教授	航天学院	A low-cost attitude and heading reference system by combination of MEMS intertial sensors and magnetometers	Proceedings of the 2009 International Conference on Information , Electronic and Computer Science	323-326 Novembe r 2009

10	杜杭 王惠南	研究生， 教授	航天学院	全息真三维显示系统	激光杂志	2009 年 30 卷 5 期
11	刘钊 王惠南	研究生， 教授	航天学院	一种改进的 Snake 模型及其在医学图像分割中的应用	科技情报开发与经济	2009 年 19 卷 26 期
12	王冬翠 王惠南	研究生， 教授	航天学院	关于立体视觉与真三维立体显示技术	现代显示	2009 年 9 期
13	刘海颖 王惠南	研究生， 教授	航天学院	卫星编队飞行的光通信研究	遥测遥控	2009 年 30 卷 5 期
14	翁晓光 王惠南	研究生， 教授	航天学院	改进的 ICA 算法及其在 fMRI 信号上的应用	华南理工大学学报：自然科学版	2009 年 37 卷 5 期
15	吕振斌 王惠南	研究生， 教授	航天学院	一种 H.264 基本单元层的码率控制算法	电视技术	2009 年 S1 期
16	冯成涛 王惠南	研究生， 教授	航天学院	磁控小卫星编队飞行的非线性控制	传感器与微系统	2009 年 28 卷 3 期
17	刘海颖 王惠南	研究生， 教授	航天学院	喷气/偏置动量轮联合微小卫星三轴稳定控制	系统仿真学报	2009 年 21 卷 7 期
18	李虹 王惠南	研究生， 教授	航天学院	血管内超声图像的血液噪声抑制和对比度增强算法	华南理工大学学报：自然科学版	2009 年 37 卷 1 期
19	张俊 王惠南	研究生， 教授	航天学院	真三维旋转显示屏体素分析及均匀化校正研究	现代显示	2009 年 1 期
20	张丽萍 王惠南	研究生， 教授	航天学院	污染环境中赤潮非线性动力学模型的稳定性分析	重庆大学学报	2009 年 32 卷 2 期
21	张焕萍 王惠南	研究生， 教授	航天学院	基于互信息的差异共表达致病基因挖掘方法	东南大学学报：自然科学版	2009 年 39 卷 1 期
22	杨志根 王惠南	研究生， 教授	航天学院	基于 ICA 的 fMRI 分析方法的成分可靠性和选择	中国医学物理学杂志	2009 年 26 卷 1 期
23	丁尚文 王惠南	研究生， 教授	航天学院	基于对偶四元数的航天器交会对接位姿视觉测量算法	宇航学报	2009 年 30 卷 6 期
24	钟元 王惠南	研究生， 教授	航天学院	Detecting functional connectivity in fMRI using PCA and regression analysis	Brain topograghy	2009 年
25	钟元 王惠南	研究生， 教授	航天学院	基于 fMRI 瞬时功率的独立成分分析	中国图象图形学报	2009 年 10 期
26	杜杭 王惠南	研究生， 教授	航天学院	利用小波变换提高数字全息信噪比	光学仪器	2009 年 31 卷 2 期
27	冷雪飞	讲师	航天学院	提高景象匹配导航系统效能的轮盘式变倍机构	第三届中国导航、制导与控制学术会议	2009.11
28	冷雪飞	讲师	航天学院	Disc Varifocal Mechanism to Improve Efficiency of Scene Matching Navigation System	Second International Conference on Future Information Technology and Management Engineering	2009.12

29	董圣男 王小涛	研究生， 讲师	航天学院	A Novel High-Speed Parallel Scheme for Data Sorting Algorithm Based on FPGA	2nd International Congress on Image and Signal Processing, CISP '09.	2009. Vol. 7
30	王小涛	讲师	航天学院	FPGA Based Parallel Architectures for Normalized Cross-Correlation	2009 First IEEE International Conference on Information Science and Engineering (ICISE2009)	
31	李爽	副教授	航天学院	Autonomous navigation and guidance scheme for precise and safe planetary landing	Aircraft Engineering and Aerospace Technology	2009 年 81 卷 6 期
32	李爽	副教授	航天学院	着陆小行星的视线测量自主光学相对导航算法及其可观性分析	航空学报	2009 年 30 卷 9 期
33	李爽	副教授	航天学院	Innovative EDL GNC Scheme for Precise and Safe Mars Landing Missions	60th International Astronautical Congress 2009 - Daejeon, South Korea	
34	李爽	副教授	航天学院	火星 EDL 导航、制导与控制技术	中国宇航学会深空探测专业委员会学术年会，海南 三亚	
35	韩艳铧	副教授	航天控制系	攻击地面机动目标的一种击顶制导策略	兵工学报	2009 年 30 卷 3 期
36	韩艳铧	副教授	航天控制系	航天器姿态控制的一种自适应方法	航天控制	2009 年 27 卷 2 期
37	韩艳铧	副教授	航天控制系	空射飞航导弹姿态控制的一种自适应方法	弹箭与制导学报	2009 年 29 卷 5 期
38	徐波	教授	航天学院	Satellite selection algorithm for combined GPS-Galileo navigation receiver	Proceedings of the 4th International Conference on Autonomous Robots and Agents	2009.2, Wellington, New Zealand pp.149-154
39	徐波	教授	航天学院	Sliding mode control of space robot formation flying	Proceedings of the 4th International Conference on Autonomous Robots and Agents	2009.2, Wellington, New Zealand pp.561-565
40	徐波	教授	航天学院	The Kinematics and Control Of Relative Attitude Pointing for Spacecraft Formation Flying	Proceedings of the 21st Chinese Control and Decision Conference	2009.6, Guilin, China pp.286-29

此为试读，需要完整PDF请访问：www.ertongbook.com

						1
41	徐波	教授	航天学院	Research on Long-term Autonomous Orbit Determination for Navigation Constellation Using Inter-satellite Orientation Observation Information	Proceedings of the International Conference on Space Information Technology	2009.11, Beijing, China pp.318-325
42	徐波	教授	航天学院	An Efficient Algorithm for Autonomous Orbit Determination of Navigation Constellation Based on Cross-link Range	Proceedings of the International Conference on Space Information Technology	2009.11, Beijing, China pp.303-310
43	南英	教授	航天学院	登月返回再入轨迹的优化设计	《宇航学报》	2009 年 卷 5 期
44	南英	教授	航天学院	自由飞行中的最优飞行轨迹	《系统仿真学报》	2009 年 卷 20 期
45	蒋　萍	中级	图书馆	"JALIS 博硕士学位论文数据库的建设实践	图书情报工作	20095309
46	殷　丽	中级	图书馆	关于 Springer 西文电子图书建库的设计方案	中国科教创新导刊	20090010
47	息秀兰	初级	图书馆	关于流通服务细节　提高读者服务质量	科技情报开发与经济	20091931
48	息秀兰	初级	图书馆	论高校图书馆读者心理与服务工作	科技信息	20090030
49	卞　卉	中级	图书馆	构建高校图书馆动态人岗匹配体系的初探	科技情报开发与经济	20090003
50	卞　卉	中级	图书馆	高校图书馆拓展训练需求分析	科技情报开发与经济	20090006
51	卞　卉	中级	图书馆	高校图书馆基于岗位素质模型的培训体系构建初探	科技情报开发与经济	20090013
52	卞　卉	中级	图书馆	缩微平片数字化工作探讨	科技情报开发与经济	20090015
53	王　蓓	初级	图书馆	高校图书馆电子阅览室服务创新方法探讨	江苏航空	200900278
54	王　蓓	初级	图书馆	论图书馆的思想教育职能	唯实	20090001
55	单冠贤	初级	图书馆	Web2.0 技术下构建学科馆员服务新模式	科技情报开发与经济	20091906
56	单冠贤	初级	图书馆	网络技术在数字图书馆中应用的关键问题	科技创新导报	20090008
57	单冠贤	初级	图书馆	浅析人际网络在企业竞争情报系统中的应用	科技创新导报	20090007
58	徐　海	初级	图书馆	基于 Windows Forms 开发的随书光盘借阅管理系统的设计与实现	光盘技术	20090086
59	刘佳音	中级	图书馆	基于资料收藏网络的机构知识库内容研究	情报探索	20090004
60	方兵旺	初级	图书馆	浅谈高校图书馆消防安全工作	科技信息	20090009
61	方兵旺	初级	图书馆	浅谈高校图书馆勤工助学工作	科技信息	20090011

62	方兵旺	初级	图书馆	浅谈高校图书馆员的职业道德建设	科技信息	20090021
63	方兵旺	初级	图书馆	浅议图书馆职业道德教育的途径	中小学图书情报世界	20090004
64	秦萍	副高	图书馆	网络环境下高校图书馆的图书借阅分析思考	科技处进发展	20090008
65	徐清华	中级	图书馆	图书馆人文精神的建设与发展	产业与科技论坛	20090802
66	张磊磊 吕静 邹小筑 寇洁	硕士 硕士 副高 工程师	图书馆 图书馆 图书馆 西飞公司	对国内电磁铆接技术研究文献的定量分析	情报技术	20092700
67	吴祥玲 邹小筑	硕士 副高	图书馆	1995-2008 年国内竞争情报基金论文计量分析	2009 年中国竞争情报第十五届年会论文集	20090000
68	朱永武 蒋仁营 梁芳 黎思文	中级 副高 中级 初级	图书馆	改革电子阅览室服务模式,构建高校图书馆学习共享空间	现代情报	20092909
69	朱永武 蒋仁营 梁芳 黎思文	中级 副高 中级 初级	图书馆	依托图书馆电子阅览室　构建学习共享空间	科技情报开发与经济	20091925

Author's personal copy

Available online at www.sciencedirect.com
ScienceDirect
Advances in Space Research 44 (2009) 836–846
ADVANCES IN SPACE RESEARCH (a COSPAR publication)
www.elsevier.com/locate/asr

A numerical model characterizing internal gravity wave propagation into the upper atmosphere

Yonghui Yu [a,*], Michael P. Hickey [b], Yinfeng Liu [a]

[a] College of Astronautics, Nanjing University of Aeronautics and Astronautics, No. 29 Yu Dao Street, Nanjing, Jiangsu 210016, PR China
[b] College of Arts and Sciences, Embry-Riddle Aeronautical University, 600 S.Clyde Morris Blvd., Daytona Beach, FL 32114, USA

Received 5 November 2008; received in revised form 23 March 2009; accepted 15 May 2009

Abstract

A new two-dimensional, time-dependent and fully nonlinear model is developed to numerically simulate plane wave motions for internal gravity waves in a non-isothermal and windy atmosphere that accounts for the dissipation due to eddy and molecular processes. The atmosphere has been treated as a well mixed total gas with a constant mean molecular weight. The effects of Rayleigh friction and Newtonian cooling are applied near the upper boundary of the model to simulate the radiation conditions as well as to act as a sponge layer; lateral boundaries are periodic over a horizontal wavelength to simulate a horizontally infinite domain. The thermal excitation to initiate upward propagating waves is spatially localized in the troposphere and is a Gaussian function of time. A time-splitting technique is applied to the finite difference equations that are derived from the Navier–Stokes equations. The time integration for these highly coupled equations is performed using an explicit second order Lax–Wendroff scheme and an implicit Newton–Raphson scheme. The wave solutions derived from the model are found to be broadly agreeable with those derived from a Wentzel–Kramers–Brillouin theory.
© 2009 COSPAR. Published by Elsevier Ltd. All rights reserved.

Keywords: Gravity waves; Numerical model; Navier–Stokes equations; Lax–Wendroff scheme; Newton–Raphson scheme; Wentzel–Kramers–Brillouin theory

1. Introduction

The upper atmosphere ubiquitously exhibits wave dynamical phenomena (Hines, 1960; Hodges, 1967, 1969; Lindzen, 1981; Holton, 1982, 1983). Visual manifestations of atmospheric gravity waves have been achieved through a wide variety of remote sensing instruments, such as all-sky CCD airglow imagers (Taylor et al., 1995a,b; Nakamura et al., 1998; Nielsen et al., 2006), lidars (Wilson et al., 1991; Mitchell et al., 1991; Whiteway and Carswell, 1995), and radars (Vincent, 1984; Nakamura et al., 1997; Manson et al., 1998). Atmospheric gravity waves have been widely studied since the seminal paper of Hines (1960). They have been recognized to play a crucial role in transporting energy and momentum from the lower atmosphere, where the most energetic wave sources are located, to the middle and upper atmosphere (Fritts, 1978; Fritts and Dunkerton, 1984; Fritts, 1984).

One such source, associated with the strong convection occurring during thunderstorms, has received considerable attention in an effort to enhance our understanding of the processes involved. Gravity wave generation by convective processes has been summarized by Fritts and Alexander (2003). Essentially, the wave generation process is modeled either through an obstacle effect (Clark et al., 1986), or by a mechanical oscillator effect (Fovell et al., 1992), or as a thermal excitation (Alexander et al., 1995; Pandya and Alexander, 1999; Piani et al., 2000). The latter mechanism, associated with the latent heat release accompanying convection, has particularly been explored through numerical modeling. Not only are planetary scale waves generated through latent heat release (Manzini and Hamilton, 1993), but also smaller scale gravity waves are produced (Walterscheid et al., 2001; Beres et al., 2004; Alexander

* Corresponding author.
E-mail addresses: yuyong@nuaa.edu.cn (Y. Yu), Michael.Hickey@erau.edu (M.P. Hickey), yinfeng@nuaa.edu.cn (Y. Liu).

0273-1177/$36.00 © 2009 COSPAR. Published by Elsevier Ltd. All rights reserved.
doi:10.1016/j.asr.2009.05.014

Author's personal copy

et al., 2004). Direct observational evidence for the latent heating mechanism of wave generation has been provided by Mclandress et al. (2000).

Confirmation of model predictions by observations is useful to the understanding of the source processes. Waves of importance to the upper mesosphere have amplitudes that are typically below the threshold of observability near the source region. In this case a comparison between observations and modeling is best performed for the faster waves that reach the mesopause region. Observational techniques, such as ground-based airglow imaging, can provide the model-needed information regarding the directions of wave propagation, the wave extrinsic periods and their horizontal wavelengths (Walterscheid et al., 1999; Hecht et al., 2001). Combined with models describing the interaction of waves with chemistry and the associated airglow emissions, such measurements provide a useful way of determining the gravity wave amplitudes, momentum fluxes, and energy fluxes (Nakamura et al., 1993; Swenson and Gardner, 1998; Gardner et al., 1999; Hickey, 2001; Hickey and Yu, 2005). Radar observations allow the momentum flux to be calculated using the method described by Vincent and Reid (1983) or by correlating the horizontal and vertical velocity (Fritts and Yuan, 1989).

In spite of the desire to reconcile models with observations the modeling itself, using advanced computational techniques to simulate the wave dynamical processes, is a valid scientific approach to help our understanding of wave generation and propagation (Lindzen, 1970; Fovell et al., 1992; Alexander et al., 1995). It has become more useful with recent computational capabilities with improvements in processor speed, increased memory and more efficient numerical algorithms. For instance, using the comprehensive SKYHI general circulation model (GCM), Manzini and Hamilton (1993) investigated the propagation through the lower and middle atmosphere of equatorial planetary waves and inertia-gravity waves excited by latent and convective heating. Their studies reconfirmed that latent and convective heating are important wave sources, and these wave sources were indicated to be a dominant mechanism in producing equatorial wave activity. In another case, Alexander et al. (1995) studied convectively forced mesoscale atmospheric gravity waves. High frequency oscillations were produced in the stratosphere above the simulated storm. They showed that their modeled gravity wave vertical wavelengths exhibited a surprisingly strong correlation with the heating depth. Spectral analysis was applied by Pandya and Alexander (1999) to further investigate the stratospheric gravity waves above convective thermal excitation. For both linear and nonlinear forcing, their simulations clearly revealed a strong resemblance between the dominant frequency of the stratospheric gravity waves and the oscillating frequency of the time-varying tropospheric thermal excitation. As we mentioned above, model simulations allow researchers to correctly interpret observational data, predict unobserved wave events, and acquire further understanding of unexplored physical processes (Hickey et al., 1997, 1998; Walterscheid and Schubert, 1990; Walterscheid et al., 2001; Snively and Pasko, 2003, 2005; Snively et al., 2007; Yu and Hickey, 2007a,b,c).

The purpose of this paper is to describe a new two-dimensional model that is based on the Navier–Stokes equations and used to simulate the propagation of atmospheric gravity waves. Briefly, the model describes the temporal evolution and spatial distribution of non-hydrostatic, nonlinear gravity waves propagating within an inhomogeneous and compressible atmosphere. The application of this model to the thermal ducting of acoustic-gravity waves in multiple ducts (in the stratosphere, mesosphere and lower thermosphere) has been described by Yu and Hickey (2007a,b). The extension of these studies to include the effects of background winds has been described by Yu and Hickey (2007c). Here, the wave solutions provided by the model will be compared to those derived from a WKB approximation. The source (and wave) amplitude in the model will be kept small in order to facilitate a meaningful comparison with the results from the WKB approximation. Some expected differences between the results will be described in Section 4.

The layout of this paper is as follows. The model equations and the major algorithms and solution techniques used are described in Section 2. The results, provided in Section 3, will include a simulation of a Gaussian wave packet propagating upward through a windy and non-isothermal atmosphere. A comparison with the WKB approximation is also described in this section. A discussion and conclusions are presented in Sections 4 and 5, respectively.

2. Model formulation

2.1. Governing equations

The governing equations solved in the model are the Navier–Stokes equations and the equation of state for an ideal gas. These highly coupled equations include dissipation due to eddy processes and molecular processes (viscosity and thermal conduction) and are used to describe time-dependent, two-dimensional, fully compressible, non-hydrostatic plane wave motions in a non-isothermal atmosphere and in the presence of background winds (Yu and Hickey, 2007c). The Coriolis force (owing to the rotation of the Earth) (Hickey, 1988a, 1988b) and ion drag (Yu and Hickey, 2007b) are negligible for the high frequency gravity waves we are studying here and so are neglected. Composition effects in the thermosphere associated with an altitude variation of the mean molecular weight (Walterscheid and Hickey, 2001) are also neglected. The atmospheric regions we are interested in are below the thermosphere and so can be treated as a well mixed single constituent gas. These topics are discussed in more detail in Section 4.

The following equations describe conservation of mass (Eq. (1)), momentum (Eq. (2)) and energy (Eq. (3)), the def-

Author's personal copy

inition of potential temperature (Eq. (4)), and the ideal gas equation of state (Eq. (5)):

$$\frac{D\rho}{Dt} + \rho\underline{\nabla}\cdot\underline{v} = 0, \tag{1}$$

$$\rho\frac{D\underline{v}}{Dt} + \underline{\nabla}p - \rho\underline{g} - \underline{\nabla}\cdot(\rho\upsilon\underline{\nabla}\underline{v}) - \underline{\nabla}\cdot(\rho\eta_e\underline{\nabla}\underline{v}) + \rho K_R\underline{v} = 0, \tag{2}$$

$$\rho c_v\frac{DT}{Dt} + p\underline{\nabla}\cdot\underline{v} - \underline{\nabla}\cdot(\lambda_m\underline{\nabla}T) - \frac{c_pT}{\theta}\underline{\nabla}\cdot(\rho\kappa_e\underline{\nabla}\theta) + c_v\rho K_NT = \rho c_v(Q_i + Q_w), \tag{3}$$

$$\theta = T/\Pi = T\left(\frac{\bar{p}_{00}}{p}\right)^{\kappa}, \tag{4}$$

$$p = \frac{\rho R^*T}{M}. \tag{5}$$

The model domain is in the x–z-plane and t is time. The model extends vertically from the ground up to the altitude of 250 km and spans horizontally one horizontal wavelength allowing periodic boundary conditions to be imposed. $\underline{v}$ is the normal velocity vector with x (positive eastward) and z (positive upward) component u and w, respectively; ρ is the atmospheric neutral density; p is the atmospheric pressure; g is the acceleration due to gravity; υ is the molecular viscosity; η_e is the eddy momentum diffusivity; c_v and c_p are the specific heats at constant volume and constant pressure, respectively (we accidentally used c_v instead of c_p in the fourth term of Eq. (4) in Yu and Hickey (2007b) and now it is used correctly); Q_i is the atmospheric heat source introduced to balance the thermodynamic energy in the initial mean state; Q_w is the wave thermal excitation; T is the atmospheric temperature; λ_m is the molecular thermal conductivity; κ_e is the eddy thermal diffusivity; M is the mean molecular weight; and K_R and K_N are Rayleigh friction and Newtonian cooling coefficients, respectively. The operator $D/Dt = \partial/\partial t + \underline{v}\cdot\underline{\nabla}$ is the substantial derivative, where $\underline{v}(x,z,t)$ is the total velocity vector (mean plus perturbation). θ is the potential temperature, Π is the exner function, $\bar{p}_{00} = 1000$ mbar (the over-bar represents a horizontal average) is the reference pressure on the ground, $\kappa = R/c_p$, $R = R^*/M$, and R^* is the universal gas constant. Other relevant parameters will be discussed in Appendix A and can also be found in Walterscheid and Schubert (1990), Hickey et al. (2000, 2003) and Hickey and Yu (2005).

2.2. Computational algorithms

The model equations are first rewritten as partial differential equations in a flux preserved form and then are integrated with respect to time using a time-splitting technique. The first half integration uses an explicit, second order Lax–Wendroff scheme for the convective part of the equations. The second half integration is performed iteratively using a Newton–Raphson scheme for the remainder of the equations. The mass continuity equation and the horizontal momentum equation are solved using the second order Lax–Wendroff scheme alone, while the thermodynamic energy equation and the vertical momentum equation use both schemes.

In order to demonstrate this approach, we use as an example the mass continuity equation (1), which is rewritten as

$$\frac{\partial\rho}{\partial t} + \frac{\partial\rho u}{\partial x} + \frac{\partial\rho w}{\partial z} + s_1 = 0, \tag{6}$$

and $s_1 = 0$. This flux preserved form of the mass continuity equation will be solved at each time step by an explicit, second order Lax–Wendroff scheme alone (discussed later). The same method, when applied to the horizontal momentum equation and using Eq. (6), allows us to rewrite Eq. (2) as

$$\frac{\partial\rho u}{\partial t} + \frac{\partial\rho uu}{\partial x} + \frac{\partial\rho uw}{\partial z} + s_4 = 0. \tag{7}$$

Here we provide an expression for the s_4 term that can be derived from the momentum equation (2),

$$s_4 = \frac{\partial p}{\partial x} + \rho K_Ru - \rho(\upsilon + \eta_e)\left(\frac{\partial^2u}{\partial x^2} + \frac{\partial^2u}{\partial z^2}\right) - \left(\frac{\partial\rho\upsilon}{\partial x} + \frac{\partial\rho\eta_e}{\partial x}\right)\frac{\partial u}{\partial x} - \left(\frac{\partial\rho\upsilon}{\partial z} + \frac{\partial\rho\eta_e}{\partial z}\right)\frac{\partial u}{\partial z}. \tag{8}$$

We emphasize again that the finite difference equations (6) and (7) will be solved by an explicit, second order Lax–Wendroff scheme alone at the beginning of each time step.

The explicit, second order Lax–Wendroff scheme used here is a commonly used method described in standard books of computational fluid dynamics. We suppose that there is a general flux preserved form for each equation written as

$$\frac{\partial\Phi}{\partial t} + \frac{\partial F}{\partial x} + \frac{\partial G}{\partial z} + S = 0, \tag{9}$$

where $\Phi = \{\rho, p, \rho w, \rho u\}$, $F = \{\rho u, pu, \rho wu, \rho uu\}$, $G = \{\rho w, pw, \rho ww, \rho uw\}$ and $S = \{s_1, s_2, s_3, s_4\}$ that depends on each individual equation. The S term is commonly referred to as the source (if negative) or sink (if positive). The Φ term is the primary variable to be solved and the F and G terms are the horizontal and vertical flux term, Φu and Φw, respectively. If we take a Taylor expansion for the primary variable Φ at time step $n+1$ that is represented as Φ_{n+1}, it should look like the following:

$$\Phi_{n+1} = \Phi_n + \Delta t\frac{\partial\Phi}{\partial t} + \frac{\Delta t^2}{2}\frac{\partial^2\Phi}{\partial t^2} + (\Delta t^3) + \cdots, \tag{10}$$

where Φ_n is the primary variable Φ at time step n, and Δt is the finite time step. The explicit, second order Lax–Wendroff scheme that we apply neglects the third (Δt^3) and the higher order terms. The second derivative term $\partial^2\Phi/\partial t^2$ can be obtained from the first derivative term $\partial\Phi/\partial t$ in Eq. (9) as

Author's personal copy

$$\frac{\partial^2 \Phi}{\partial t^2} = -\frac{\partial}{\partial x}\left(\frac{\partial F}{\partial t}\right) - \frac{\partial}{\partial z}\left(\frac{\partial G}{\partial t}\right) - \frac{\partial S}{\partial t}, \tag{11}$$

so that the primary variable Φ can be solved at each successive time step once the initial condition is established. In our simulation, we have included initial tendency.

The vertical momentum equation is also rewritten in a general flux preserved form following an approach similar to that just applied to the horizontal momentum equation (7). We re-emphasize that a time-splitting technique is applied to the vertical momentum equation and also to the thermodynamic energy equation. In the thermodynamic energy equation (3), we use Eq. (4) to eliminate the potential temperature θ, and then use Eq. (5) to eliminate the atmospheric temperature T by replacing it with the atmospheric pressure p. Both the vertical momentum equation and the thermodynamic energy equation are split into two parts of the form

$$\frac{\partial \Phi}{\partial t} = f_i(\Phi) + f_e(\Phi), \tag{12}$$

where f_i represents those terms evaluated implicitly by the Newton–Raphson scheme, and f_e represents those terms evaluated explicitly by the Lax–Wendroff scheme.

For the vertical momentum equation, f_e is represented as

$$\frac{\partial \rho w}{\partial t} + \frac{\partial \rho w u}{\partial x} + \frac{\partial \rho w w}{\partial z} + s_3 = 0, \tag{13}$$

where the explicit representation of the s_3 term is derived from the momentum equation (2) and provided below in a form similar to (8):

$$s_3 = \rho K_R w - \rho(\upsilon + \eta_e)\left(\frac{\partial^2 w}{\partial x^2} + \frac{\partial^2 w}{\partial z^2}\right) - \left(\frac{\partial \rho \upsilon}{\partial x} + \frac{\partial \rho \eta_e}{\partial x}\right)\frac{\partial w}{\partial x} - \left(\frac{\partial \rho \upsilon}{\partial z} + \frac{\partial \rho \eta_e}{\partial z}\right)\frac{\partial w}{\partial z}. \tag{14}$$

All the terms in Eq. (14) will be included in the second order Lax–Wendroff scheme to be solved. We exclude the hydrostatic balance terms ($\partial p/\partial z - \rho g$) from Eq. (14) because they will be included in the implicit term f_i and will be iteratively solved by the Newton–Raphson scheme.

For the thermodynamic energy equation, f_e is represented as

$$\frac{\partial p}{\partial t} + \frac{\partial p u}{\partial x} + \frac{\partial p w}{\partial z} + s_2 = 0. \tag{15}$$

The s_2 term is derived from the thermodynamic energy equation (3) and provided as

$$s_2 = pK_N + (\gamma - 1)\left\{p\frac{\partial u}{\partial x} - \underline{\nabla}\cdot\left(\lambda_m \underline{\nabla}\frac{pM}{\rho R^*}\right) - c_p\left(\frac{p}{\bar{p}_{00}}\right)^{\kappa}\underline{\nabla}\cdot\left[\rho\kappa_e\underline{\nabla}\left(\frac{pM}{\rho R^*}\left(\frac{\bar{p}_{00}}{p}\right)^{\kappa}\right)\right]\right\}, \tag{16}$$

where γ is the ratio of the specific heats (c_p/c_v). We include $(\gamma - 1)p\partial w/\partial z$ in the f_i term that will be evaluated implicitly by the Newton–Raphson scheme. The diffusion terms are also included in the f_i term that will be solved by the implicit Newton–Raphson scheme, because they eliminate abruptly changing solutions and so help reduce the computation time required to achieve convergence. We set up a suitable tolerated error to iterate in the implicit Newton–Raphson scheme to make sure the same order accuracy between the implicit and explicit scheme. A detailed description of the implicit Newton–Raphson scheme is provided by Press et al. (1996).

We use the traditional Courant–Friedrichs–Lewy stability criterion to set time steps for the proposed algorithms. The requirement for the time and space step is

$$\frac{|v|\Delta t}{\Delta x} \leqslant 1. \tag{17}$$

The horizontal and vertical grid spacing (Δx and Δz) used in the proposed algorithms are 0.5 km and 1.0 km, respectively. The time step (Δt) is 0.7 s. They satisfy the CFL condition (17) even for the fast acoustic wave (about 300 m/s).

The primary wave variables (ρ, p, ρw, ρu) are solved using a staggered grid technique similar to that described by Taylor (1984). In this technique the atmospheric density (ρ) and pressure (p) or temperature (T) are carried on one grid system, while the horizontal and vertical mass flux term (ρu and ρw) are computed on another grid system that is purposely staggered with respect to the former by a half-unit spatial step both in the horizontal and vertical direction. Equivalently, this means that the atmospheric density and pressure (or temperature) are carried at the center of a computational unit box, while the horizontal and vertical mass flux term (ρu and ρw) are computed at the midpoints of the lateral and vertical boundaries of a computational unit box, respectively. A similar application has been described by Walterscheid and Schubert (1990). A periodic boundary condition applies to the lateral boundaries to simulate a horizontally infinite domain. On the ground the vertical velocity is set to zero to ensure that there are no wave fluxes through the lowest boundary.

3. Model simulations

The simulations use thermal forcing described as a sinusoid in time modulated by a Gaussian function in time and in the vertical coordinate. These simulations are apt to mimic what might be expected by a thunderstorm source of waves. The thermal forcing in the thermodynamic energy equation (3) is described as a traveling sine wave with an amplitude modulated by a Gaussian function in the vertical coordinate.

3.1. Gaussian wave packet simulations

In general any reasonable combination of wave parameters can be input to the model. Here, a wave thermal excitation with a primary period of 6.276 min and a horizontal wavelength of 35 km is chosen that are based on previous applications of the full-wave model to wave ducting (Hecht et al., 2001). These earlier results obtained with the full-

此为试读,需要完整PDF请访问: www.ertongbook.com

Author's personal copy

wave model indicate that this wave mode is strongly ducted in the lower thermospheric thermal duct. Our purpose of providing a specific wave source is trying to test the model sensitivity and to see whether or not the model could characterize the wave propagating properties correctly within the linear gravity wave theory. This wave thermal excitation is a sinusoidal function in the horizontal direction and is periodic over the domain. It is characterized by a Gaussian envelop of half-width $\Delta z = 0.8$ km, centered vertically at $\xi = 8$ km, and a Gaussian envelop of half-width $\Delta t = 6.276$ min, centered temporally at $\tau = 37.656$ min. The magnitude of the thermal forcing is maintained small enough (10^{-5} K/s) to ensure that the gravity wave amplitudes remain linear at all heights. The thermal excitation is expressed analytically as

$$Q_w(x,z,t) = 10^{-5}\exp(-(t-\tau)^2/2\Delta t^2) \times \exp(-(z-\xi)^2/2\Delta z^2)\sin(k_0 x - \omega_0 t). \quad (18)$$

The thermal forcing frequency and the horizontal wave number are given by $\omega_0 = 2\pi/6.276$ min and $k_0 = 2\pi/35$ km, respectively. Positive k_0 represents eastward propagating waves.

The thermal excitation and the fractional temperature perturbation at a horizontal position of $x = 17.25$ km and at an altitude of $z = 8$ km (the height of maximum wave forcing) are shown in the right panel of Fig. 1. The thermal excitation and the resulting fractional temperature perturbation vary with time in a similar way, with the thermal excitation leading the fractional temperature perturbation by a phase of approximate $\pi/2$ (about 1/4 of the forcing period of 6.276 min). The wave excitation has a primary period of about 6.17 min and is centered at about 36.17 min; the fractional temperature perturbation has a primary period of about 6.33 min and is centered at about 37.67 min. Therefore there is a delay of approximate 1/4 wave major period (6.276 min) between the effect (the fractional temperature perturbation) and the cause (the thermal excitation). When the thermal forcing is a maximum the fractional temperature perturbation is zero, and when the thermal forcing is zero the fractional temperature perturbation is a maximum.

In the left panel of Fig. 1, we plot the zonal wind (upper x-axis, positive eastward) as a function of altitude. We also plot the thermal conductivity and the momentum diffusivity that will be discussed later in Appendix A. The atmospheric mean temperature that determines the Brunt–Väisälä frequency and the atmospheric mean density are prescribed using the MSIS-E-90 model (Hedin, 1991) for a date of 1993 January 15, a location of latitude N 18.5° and longitude 0.0°, and a local time of 2200 h. The zonal wind structure is prescribed using the Horizontal Wind Model (HWM93) (Hedin et al., 1996) for the same geophysical parameters.

As shown in the left panel of Fig. 1, the zonal wind has a positive wind shear ($dU/dz > 0$) in three regions: from $z = 0$ to $z = \sim 12.5$ km, from $z = \sim 43.5$ km to $z = \sim 72.5$ km, and from $z = \sim 98.5$ km to $z = \sim 117.5$ km. The zonal wind also

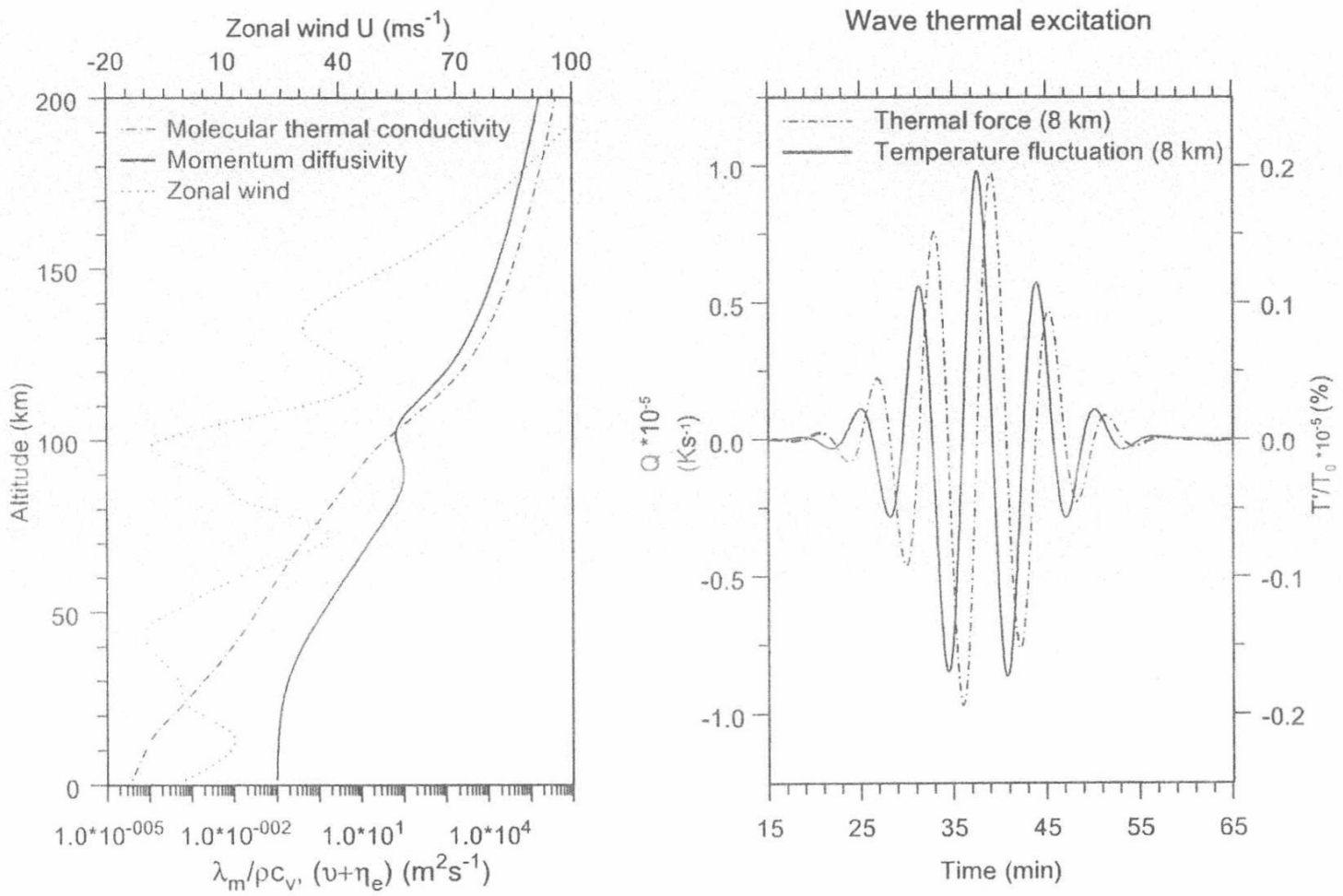

Fig. 1. Molecular thermal conductivity ($\lambda_m/\rho c_v$, dash–dot curve), momentum diffusivity ($\upsilon + \eta_e$, solid curve) and the zonal wind (U, dot curve, positive eastward) are shown on the left panel. The thermal excitation (Q, dash–dot curve) and the temperature fluctuation (T'/T_0, solid curve) at $z = 8$ km are shown on the right panel.

has a negative wind shear ($dU/dz < 0$) in three regions: from $z = \sim 12.5$ km to $z = \sim 43.5$ km, from $z = \sim 72.5$ km to $z = \sim 98.5$ km, and from $z = \sim 117.5$ km to $z = \sim 133.5$ km. From $z = \sim 133.5$ km the zonal wind continues to increase up to the model upper boundary. The wave packet propagates upward and eastward from the source (at $z = 8$ km) with a horizontal phase speed of about 92.95 m/s ($V_p = \omega_0 / k_0$). At altitudes of about 12.5 km, 72.5 km and 117.5 km, where the zonal wind is a local eastward maximum, the wave experiences a tail wind. In this case the wave is Doppler shifted to lower frequencies according to the equation $\Omega = \omega - \underline{k} \cdot \underline{U}$, where Ω is the Doppler shifted frequency, ω is the extrinsic frequency observed on the ground, $\underline{k}$ is the horizontal wave number and $\underline{U}$ is the zonal wind. At altitudes of about 43.5 km and 98.5 km where the zonal wind reaches a local westward maximum, the wave experiences a head wind and is Doppler shifted to higher frequencies.

Figs. 2–5 show the wave fluctuations in the atmospheric density, temperature, horizontal velocity and vertical velocity at four different times of about 47 min, 1 h 9 min, 1 h 31 min, and 5 h 48 min. The scaling in these four figures is not identical. Fig. 2 is a snapshot of the fractional density perturbation ρ'/ρ_0 (unit: %) at 47 min and 4 s. Regions of maximum tail wind and head wind are shown in this figure by the horizontal dashed lines. In the tail wind regions where the wave is Doppler shifted to lower frequencies the local vertical wavelength decreases, while in the head wind regions where the wave is Doppler shifted to higher frequencies the local vertical wavelength increases. This behavior is expected based on the dispersion equation for atmospheric gravity waves (Hines, 1960).

Similar wind shear effects described in Fig. 2 can also be seen in Fig. 3 with the fractional temperature perturbation T'/T_0 (unit: %) at 1 h 9 min. Again, in the tail wind regions where the waves become slower the vertical wavelengths are shorter, whereas in the head wind regions where the waves become faster the vertical wavelengths are larger.

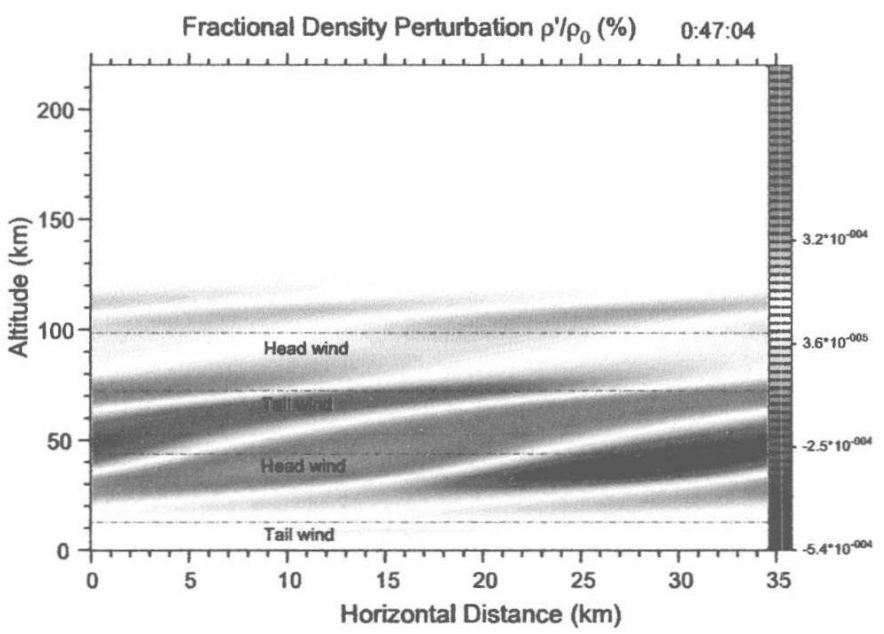

Fig. 2. A spatially localized fractional density perturbation ρ'/ρ_0 (%) is shown at a simulated time of 47 min and 4 s.

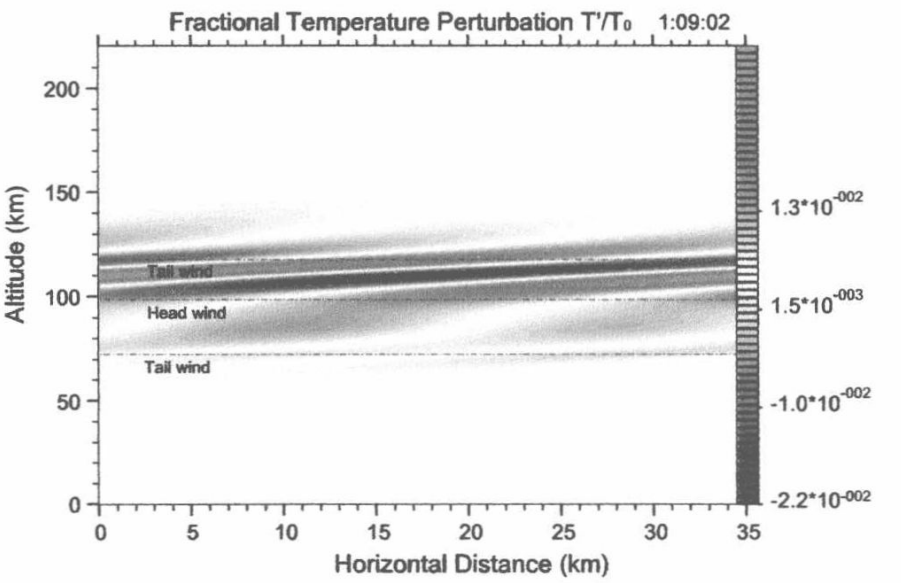

Fig. 3. A spatially localized fractional temperature perturbation T/T_0 (%) is shown at a simulated time of 1 h, 9 min and 2 s.

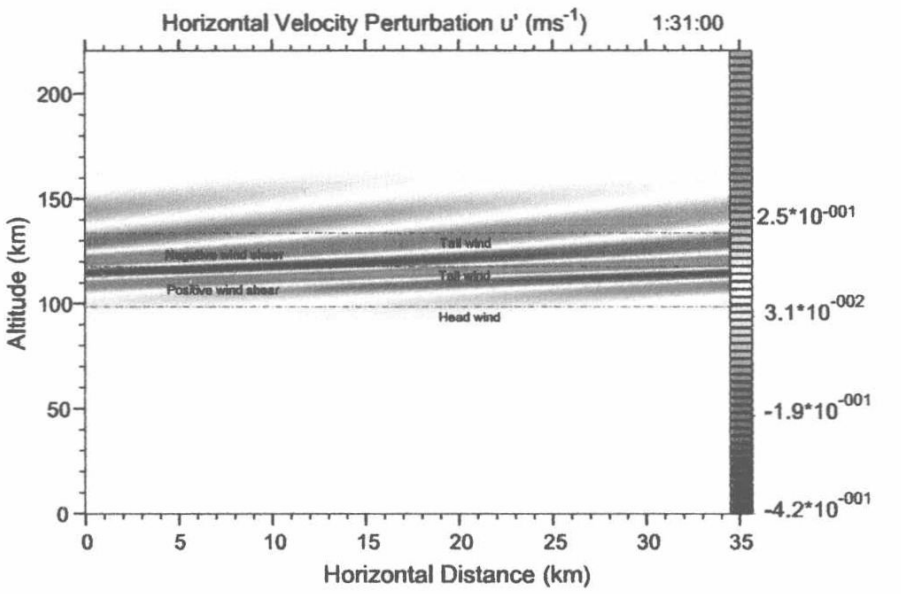

Fig. 4. A spatially localized horizontal velocity perturbation u' (m s^{-1}) is shown at a simulated time of 1 h and 31 min.

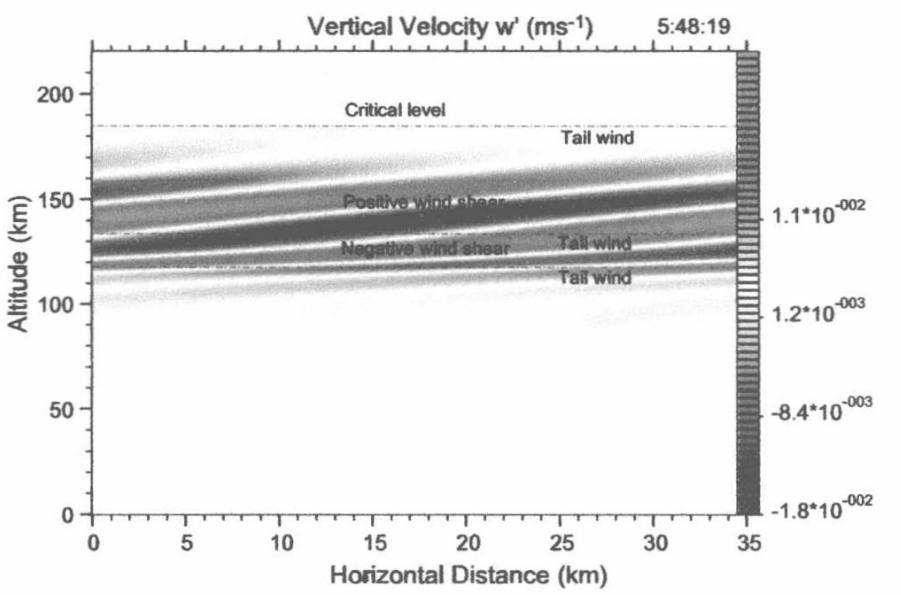

Fig. 5. A spatially localized vertical velocity w' (m s^{-1}) is shown at a simulated time of 5 h, 48 min and 19 s.

In Fig. 4 we show the horizontal velocity perturbation at 1 h and 31 min. The waves experience a local maximum headwind at ~98.5 km altitude. Above ~105 km the zonal wind becomes eastward and the waves experience a tail

wind. The eastward winds first increase with increasing altitude ($d\overline{U}/dz > 0$) and a maximum eastward tailwind occurs at ~117.5 km altitude. At greater heights the eastward wind decreases ($d\overline{U}/dz < 0$) but it remains eastward. Hence the waves experience a weaker tailwind at heights above 117.5 km. At these greater heights the vertical wavelength (~25 km) is therefore greater than that at 117.5 km altitude (~15 km). This can be seen in the figure by comparing the slopes of the lines of constant phase. This behavior is also expected based on the dispersion equation for atmospheric gravity waves (Hines, 1960).

In Fig. 5 we show the vertical velocity at ~5 h, 48 min. In the upper region of the model ($z > 133.5$ km altitude), the wind shear is positive. By ~185 km altitude the zonal wind speed has increased sufficiently to produce a critical level where the zonal wind speed equals the horizontal phase speed (~92.95 m/s) of the primary wave (see the left panel of Fig. 1). At the critical level the waves cease their upward propagation because of their zero intrinsic (Doppler shifted) frequency, and the wave associated momentum and energy are absorbed by the mean flow.

The velocity correlation $u'w'$, once averaged ($\overline{u'w'}$) (unit: $m^2\,s^{-2}$, the momentum flux per unit density), represents the vertical flux of the horizontal momentum carried by the upward propagating waves. Fig. 6 is a snapshot across the spatial grid at a time of ~47 min for a spatially localized $u'w'$. This second order, nonlinear quantity shows how the wave propagates upward in the atmosphere and it has two maxima within a horizontal wavelength. The kinetic energy density $(u'^2 + w'^2)/2$ (unit: J kg^{-1}, the energy per unit mass) can be used to estimate the kinetic energy carried by the waves. Fig. 7 is a snapshot across the spatial grid at a time of 47 min and 4 s for a spatially localized $(u'^2 + w'^2)/2$. This second order, nonlinear quantity also shows how the wave associated kinetic energy propagates upward in the atmosphere and it also has two maxima within a horizontal wavelength. The kinetic energy (Fig. 7) and the horizontal momentum (Fig. 6) both exhibit similar propagating characteristics.

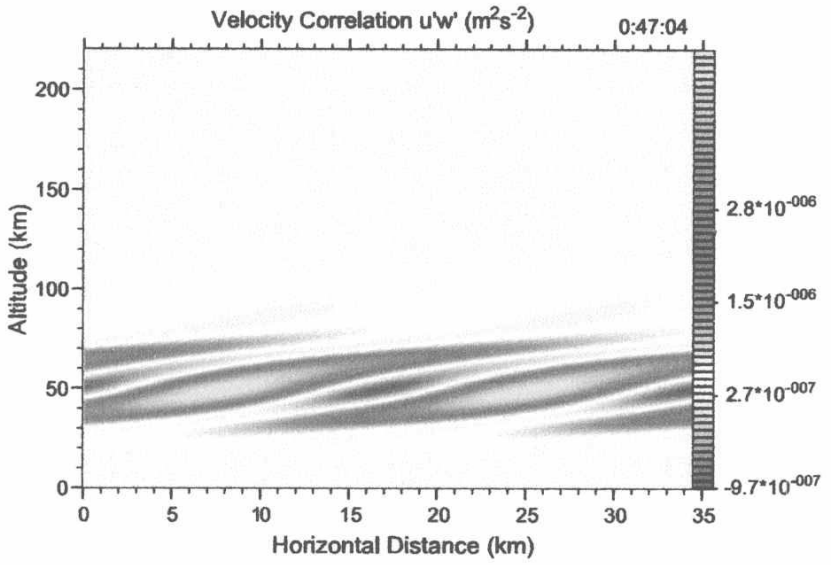

Fig. 6. A spatially localized velocity correlation $u'w'$ ($m^2\,s^{-2}$) is shown across the spatial grid at a simulated time of 47 min and 4 s.

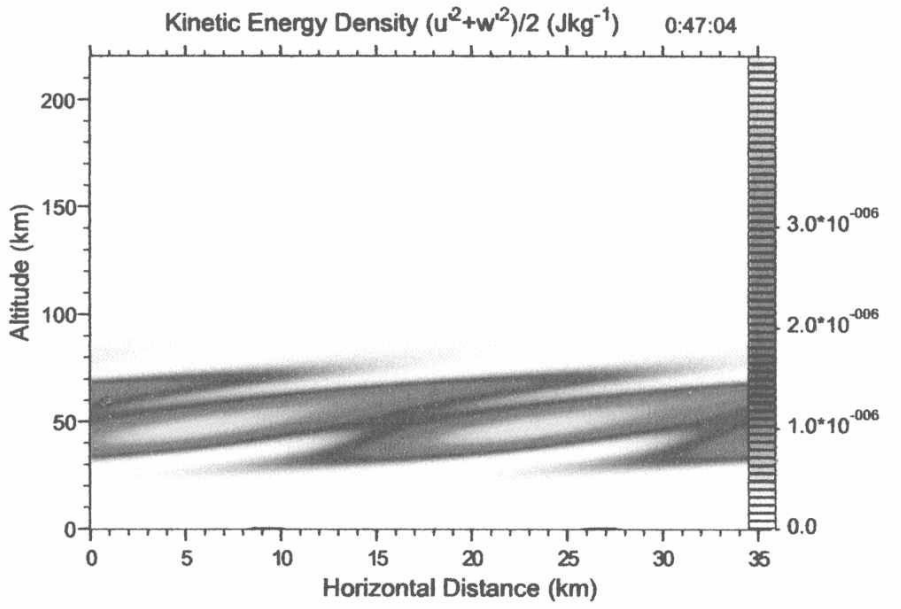

Fig. 7. A spatially localized kinetic energy density $(u'^2 + w'^2)/2$ (J kg^{-1}) is shown across the spatial grid at a simulated time of 47 min and 4 s.

3.2. Analytical comparisons

The dispersion relation formulated by Hines (1960) involves thermal and wind effects in a WKB approximation (Einaudi and Hines, 1971), and can be solved for the square of the vertical wave number (m^2) thus

$$m^2 = k^2\left(\frac{N^2}{\Omega^2} - 1\right) - \frac{(\omega_a^2 - \Omega^2)}{C^2}. \tag{19}$$

Here $\Omega = \omega - k \cdot \underline{\bar{U}}$ is the intrinsic (Doppler shifted) frequency, ω is the extrinsic (ground based) frequency, $\underline{k}$ is the horizontal wave number vector, $\underline{\bar{U}}$ is the horizontal mean wind vector. The effects of wind shear are implicitly included in Ω due to its dependence on $\underline{\bar{U}}$. The sound speed $C = \sqrt{\gamma g H}$, where γ is the ratio of the specific heats, g is the gravitational acceleration, $H = RT/g$ is the atmospheric scale height, and where R is the gas constant, and T is the atmospheric temperature (also a function of altitude). N is the Brunt–Väisälä frequency. The effects of thermal gradient are also implicitly included in the definition of the non-isothermal Brunt–Väisälä frequency (Fritts, 1984), $N^2 = (\partial T/\partial z + g/c_p)g/T$, where c_p is the specific heat at constant pressure. $\omega_a = \sqrt{\gamma g/4H}$ is the acoustic cutoff frequency.

The wave packet energy is transported at the wave group velocity ($\partial\Omega/\partial m$), which can be derived using Eq. (19) to give

$$\frac{\partial\Omega}{\partial m} = \frac{m\Omega^3}{(\Omega^4/C^2 - k^2N^2)}. \tag{20}$$

In Table 1, we calculate the vertical group velocity as a function of altitude from $z = 15.5$ km to $z = 39.5$ km using Eqs. (19) and (20) for the same mean state conditions as before. It is important to note that the phase of a freely propagating gravity wave is downward for upward energy propagation, which means that the vertical wave number m is negative. In this calculation, we specify the parameters as follows: $\omega = 2\pi/(6.276*60)$ (s^{-1}), $k = 2\pi/(35*1000)$

Table 1
The vertical group velocity derived from a WKB approximation.

Altitude (km)	Temperature (K)	Zonal wind (m/s)	Vertical group velocity (m/s)
14.5	203.83		
15.5	201.58	11.592	39.087
16.5	201.20	10.390	40.196
17.5	202.22	8.929	40.881
18.5	204.19	7.311	41.762
19.5	206.67	5.639	42.865
20.5	209.20	4.016	44.014
21.5	211.54	2.542	44.993
22.5	213.72	1.321	45.713
23.5	215.76	0.429	46.171
24.5	217.71	−0.164	46.434
25.5	219.61	−0.536	46.581
26.5	221.50	−0.762	46.682
27.5	223.45	−0.920	46.783
28.5	225.49	−1.084	46.919
29.5	227.69	−1.332	47.135
30.5	230.11	−1.737	47.453
31.5	232.81	−2.283	47.875
32.5	235.88	−2.937	48.306
33.5	239.13	−3.679	48.634
34.5	242.34	−4.487	48.843
35.5	245.48	−5.342	48.940
36.5	248.52	−6.222	48.882
37.5	251.44	−7.107	48.606
38.5	254.20	−7.951	48.033
39.5	256.77	−8.749	47.115
40.5	259.13		

(m^{-1}), $g = 9.793$ $(m^2\,s^{-1})$, $R = 287.290$ $(J\,kg^{-1}\,K^{-1})$, $c_p = 1004.0$ $(J\,kg^{-1}\,K^{-1})$, and $\gamma = 1.40$.

In order to compare the model simulations with the results derived from the linear gravity wave theory, we resolve the total perturbation energy flux of the eastward propagating waves over altitude and time. The total perturbation energy flux plotted in Fig. 8 is also defined as $F_T = \overline{p'w'} + \rho_0\bar{U}\overline{u'w'}$ (Hines and Reddy, 1967; Hickey and Brown, 2002; Yu and Hickey, 2007c). In an atmosphere free of dissipation a form of the total perturbation energy flux above is a conserved quantity for gravity waves propagating through regions of wind shear. The contribution of the momentum flux (e.g., $\rho_0\bar{U}\overline{u'w'}$) can be thought of as a consequence of a coupling between the waves and the mean flow (Hines and Reddy, 1967). This form of the total perturbation energy flux, which is influenced by a horizontal zonal wind in an altitude–time domain, shows that how fast the wave energy can propagate upward into the upper atmosphere. This color contour plot demonstrates the direction of the propagating wave energy with green color indicating upward direction and blue color indicating downward direction. In particular, we color the atmospheric region in the stratosphere largely below about 39.5 km altitude with yellow to elucidate the propagation of the main wave packet during the first 50-min simulation. We partition this stratospheric region into two parts, one is above the 19.5 km altitude and below the 39.5 km altitude, and another one is below the 19.5 km altitude.

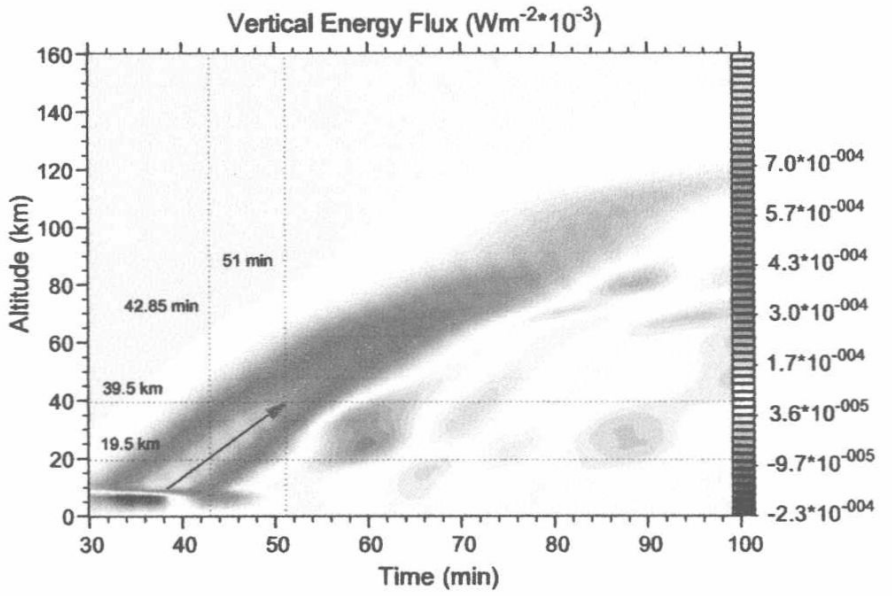

Fig. 8. The total perturbation energy flux $F_T = \overline{p'w'} + \rho_0\bar{U}\overline{u'w'}$ is shown for the eastward propagation. Two horizontal reference lines (red, dot–dot), respectively, locate at $z = 19.5$ km and $z = 39.5$ km; two vertical reference lines (red, dot–dot), respectively, locate at $t = 42.85$ min and $t = 51$ min. A red arrow points at the point ($t = 51$ min, $z = 39.5$ km) and crosses through the point ($t = 42.85$ min, $z = 19.5$ km). (For interpretation of the references to color in this figure legend, the reader is referred to the web version of this paper.)

A red arrow is used to represent the vertical group velocity of the upward propagating wave energy. According to the simulations in Fig. 8 this red arrow crosses through two points (one at $t = 42.85$ min, $z = 19.5$ km, and another one at $t = 51$ min, $z = 39.5$ km), giving a modeled vertical group velocity of about 40.9 m/s. In Table 1 we present the vertical group velocity that is based on the linear gravity wave theory (Eq. (20)). Below 19.5 km altitude the average vertical group velocity is about 41.0 m/s. However, between 19.5 km and 39.5 km altitude the vertical group velocity based on the linear gravity wave theory is ~47 m/s, which is higher than the simulated vertical group velocity (~40.9 m/s) in this stratospheric region. We attribute this discrepancy largely due to the partial reflections of the higher frequency wave components of the packet by the evanescent region at the upper stratosphere. These partial reflections can be seen in the simulation results of Fig. 8 between about $t = 53$ min and $t = 64$ min and between the altitudes of 19.5 km and 39.5 km (blue downward reflections). Because the higher frequency components of the packet are also the faster components, their partial reflections remove them from the upward propagating packet and hence reduce the vertical group velocity of the main wave packet. The vertical group velocity based on the linear gravity wave theory (Table 1) reasonably describes the freely propagating waves below 19.5 km altitude, while that based on the model simulations more reasonably describes the freely propagating and ducting waves between 19.5 km and 39.5 km altitude.

4. Discussion

In this study we deliberately chose the amplitude of the wave thermal excitation in the model to be small so that the

Author's personal copy

nonlinear terms in the governing equations would be negligible. At higher altitudes, the upper atmosphere (particularly for the thermosphere) is diffusively separated and it behaves as a multi-constituent gas. In contrast the atmospheric region below the thermosphere is considered to be well mixed, and behaves as a single constituent gas with constant molecular weight up to the turbopause (near 105 km altitude). The composition and specific heats of the total gas can be significantly different between the lower and upper atmosphere, and the parcel buoyancy can be significantly affected (Walterscheid and Hickey, 2001). These effects are beyond the scope of our present study, but we note that they may be important for the characteristics of the propagating waves discussed in this paper.

In an atmosphere with slowly varying background temperature and winds, a ray tracing method could be used to model the path taken by the propagating gravity waves. This ray tracing theory can predict where the internal gravity waves are propagating and breaking. Its successful atmospheric applications can be found, for example, in the GROGRAT model of Marks and Eckermann (1995) and Eckermann and Marks (1997), and the model of Walterscheid (2000). The GROGRAT model has been used extensively by Eckermann and colleagues to interpret satellite measurements of wave motions. We developed our present model based on our planned future science projects. For instance, calculating the nonlinear forcing and the temporal evolution of the mean state and simulating the interaction between dynamics and chemistry are more easily accomplished with this newly developed model.

5. Conclusion

A numerical modeling study of atmospheric gravity wave propagation and trapping has been performed using a relatively new time-dependent model. Group velocities derived from the model with small amplitude forcing were found to compare favorably at lower altitudes with those derived from a linear, WKB based dispersion equation. Differences at greater altitudes were attributed to dissipation and to partial reflections of larger vertical wavelength (faster) waves that are not well described by a WKB approach (Einaudi and Hines, 1971).

The model also revealed wave ducting in the middle atmosphere and lower thermosphere. The anisotropy due to mean horizontal winds was shown to be significant and affected vertical variations of phase in a predictable way. Based on the model applications performed in this paper and in some previous studies (Yu and Hickey 2007a,b,c), we believe that the newly developed model can properly characterize the upward propagation of atmospheric gravity waves into the upper atmosphere. The time-dependence and its non-linearability supported by the model provide a broad opportunity to explore some unusual wave events (for example, the mesospheric bore), and to interpret airglow observations more objectively in the case of coupling this dynamical model with an airglow chemistry model.

Acknowledgments

Michael P. Hickey was supported by the National Science Foundation under Grant ATM-0639293 to Embry-Riddle Aeronautical University. Yonghui Yu was supported by the National Natural Science Foundation of China under Grant 40874100 to Nanjing University of Aeronautics and Astronautics. We thank the reviewers for their useful comments.

Appendix A. Model coefficients

The molecular diffusion coefficients used in the governing equations are taken from Rees (1989). In a dissipative atmosphere, we apply molecular process involving molecular kinematic viscosity υ (units in $m^2\,s^{-1}$), which is expressed numerically as (Hickey and Yu, 2005)

$$\upsilon = \frac{[N_2]\times 3.43 + [O_2]\times 4.03 + [O]\times 3.90}{\rho_0 \times ([N_2]+[O_2]+[O])} \times (T_0)^{0.69} \times 10^{-7}. \quad \text{(A1)}$$

Brackets [] in the equation denote the density of the major or minor species and they are functions of altitude. ρ_0 is the atmospheric mean density and T_0 is the atmospheric mean temperature, both of them are also functions of altitude. Another molecular process is due to the molecular thermal conductivity, λ_m, that is also expressed numerically as (Hickey and Yu, 2005)

$$\lambda_m = \frac{[N_2]\times 56.0 + [O_2]\times 56.0 + [O]\times 75.90}{([N_2]+[O_2]+[O])} \times (T_0)^{0.69} \times 10^{-5}, \quad \text{(A2)}$$

and it is plotted in the left panel of Fig. 1 as $\lambda_m/\rho c_v$ (units in $m^2\,s^{-1}$).

The nominal eddy diffusion coefficients are based on a profile due to Strobel (1989) and have large values in the mesopause region. The eddy momentum diffusivity maximizes with a value of $100\,m^2\,s^{-1}$ at 90 km altitude, and the Prandtl number is 3. This maximum value for the eddy diffusivity is comparable to values derived from radar inferences of turbulent energy dissipation rates (Hocking, 1987). Similar values have also been derived from two years of continuous radar measurements near Adelaide, Australia (Hocking, 1988). A small value of eddy diffusivity ($0.1\,m^2\,s^{-1}$) is used for the lower atmosphere (below about 50 km altitude). Eddy diffusion processes involve the eddy momentum diffusivity that is expressed numerically as (Hickey and Yu, 2005)

$$\eta_e = 100\,\mathrm{sec}\,h(2.6\times(z(\mathrm{km})-90.0)/20)+0.1. \quad \text{(A3)}$$

We plot the molecular kinematic viscosity υ plus the eddy momentum diffusivity η_e ($\upsilon+\eta_e$, units in $m^2\,s^{-1}$) in the left panel of Fig. 1 as a function of altitude. Another eddy diffu-

Author's personal copy

sion process is due to the eddy thermal diffusivity $\kappa_e = \eta_e/3$ (units in $m^2\ s^{-1}$), where we consider the Prandtl number as 3 and the plot for κ_e is neglected because of its similarity to η_e.

Rayleigh friction and Newtonian cooling coefficients (units in s^{-1}) share a numerical function of altitude and provide an artificial sponge layer near the upper boundary to simulate the radiation conditions. They have large effects near the upper boundary and exponentially decrease with lower altitudes away from the upper boundary.

$$K_R = K_N = \omega \exp[(z - 250\ \text{km})/7\ \text{km}], \tag{A4}$$

where ω is the primary wave frequency and z is the altitude.

Slip boundary conditions on the lower boundary ($z = 0$) are (Lindzen, 1970)

$$\frac{d}{dz}(u', w', T') = c_s(u', w', T'), \tag{A5}$$

where

$$c_s = 1.7 \times 10^{-2}\ \text{ms}^{-1}/\upsilon(z = 0), \tag{A6}$$

where υ ($z = 0$, units in $m^2\ s^{-1}$) is the molecular kinematic viscosity on the ground (see Eq. (A1)). In our simulations the results derived from the thermal excitation centered at the altitude of 8 km are insensitive to the boundary conditions from the lower boundary.

References

Alexander, M.J., Holton, J.R., Durran, D.R. The gravity wave response above deep convection in a squall line simulation. J. Atmos. Sci. 52, 2212–2226, 1995.

Alexander, M.J., May, P.T., Beres, J.H. Gravity waves generated by convection in the Darwin area during the Darwin Area Wave Experiment. J. Geophys. Res. 109, D20S04, doi:10.1029/2004JD004729, 2004.

Beres, J.H., Alexander, M.J., Holton, J.R. A method of specifying the gravity wave spectrum above convection based on latent heating properties and background wind. J. Atmos. Sci. 61, 324–337, 2004.

Clark, T.L., Hauf, T., Kuettner, J.P. Convectively forced internal gravity waves: results from two-dimensional numerical experiments. Q. J. R. Meteorol. Soc. 112, 899–925, 1986.

Eckermann, S.D., Marks, C.J. GROGRAT: a new model of the global propagation and dissipation of atmospheric gravity waves. Adv. Space Res. 20 (6), 1253–1256, 1997.

Einaudi, F., Hines, C.O. WKB approximation in application to acoustic-gravity waves. Can. J. Phys. 48, 1458–1471, 1971.

Fovell, R., Durran, D., Holton, J.R. Numerical simulations of convectively generated stratospheric gravity waves. J. Atmos. Sci. 49, 1427–1442, 1992.

Fritts, D.C. The nonlinear gravity wave–critical level interaction. J. Atmos. Sci. 35, 397–413, 1978.

Fritts, D.C. Gravity wave saturation in the middle atmosphere: a review of theory and observations. Rev. Geophys. 22, 275–308, 1984.

Fritts, D.C., Alexander, M.J. Gravity wave dynamics and effects in the middle atmosphere. Rev. Geophys. 41 (1), 1003, doi:10.1029/2001RG000106, 2003.

Fritts, D.C., Dunkerton, T.J. A quasi-linear study of gravity wave saturation and self-acceleration. J. Atmos. Sci. 41, 3272–3288, 1984.

Fritts, D.C., Yuan, L. Measurement of momentum fluxes near the summer mesopause at Poker Flat, Alaska. J. Atmos. Sci. 46, 2569–2579, 1989.

Gardner, C.S., Gulati, K., Zhao, Y., Swenson, G. Measuring gravity wave momentum fluxes with airglow imagers. J. Geophys. Res. 104 (D10), 11903–11916, 1999.

Hecht, J.H., Walterscheid, R.L., Hickey, M.P., Franke, S.J. Climatology and modeling of quasi-monochromatic atmospheric gravity waves observed over Urbana Illinois. J. Geophys. Res. 106 (D6), 5181–5196, 2001.

Hedin, A.E. Extension of the MSIS thermosphere model into the middle and lower atmosphere. J. Geophys. Res. 96 (A2), 1159–1172, 1991.

Hedin, A.E. et al. Empirical wind model for the upper, middle and lower atmosphere. J. Atmos. Terr. Phys. 58, 1421–1447, 1996.

Hickey, M.P. Effects of eddy viscosity and thermal conduction and Coriolis force in the dynamics of gravity wave driven fluctuations in the OH nightglow. J. Geophys. Res. 93 (A5), 4077–4088, 1988a.

Hickey, M.P. Wavelength dependence of eddy dissipation and Coriolis force in the dynamics of gravity wave driven fluctuations in the OH nightglow. J. Geophys. Res. 93 (A5), 4089–4101, 1988b.

Hickey, M.P. Airglow variations associated with nonideal ducting of gravity waves in the lower thermosphere region. J. Geophys. Res. 106 (D16), 17907–17918, 2001.

Hickey, M.P., Brown, J.S. A simulation study of space-based observations of gravity waves in the airglow using observed ALOHA-93 wave parameters. J. Geophys. Res. 107 (A12), 1431, doi:10.1029/2001JA009225, 2002.

Hickey, M.P., Yu, Y. A full-wave investigation of the use of a "cancellation factor" in gravity wave–OH airglow interaction studies. J. Geophys. Res. 110, A01301, doi:10.1029/2003JA010372, 2005.

Hickey, M.P., Walterscheid, R.L., Taylor, M.J., Ward, W., Schubert, G., Zhou, Q., Garcia, F., Kelly, M.C., Shepherd, G.G. Numerical simulations of gravity waves imaged over Arecibo during the 10-day January 1993 campaign. J. Geophys. Res. 102 (A6), 11475–11490, 1997.

Hickey, M.P., Taylor, M.J., Gardner, C.S., Gibbons, C.R. Full-wave modeling of small-scale gravity waves using Airborne Lidar and Observations of the Hawaiian Airglow (ALOHA-93) O(^{1}S) images and coincident Na wind/temperature lidar measurements. J. Geophys. Res. 103 (D6), 6439–6454, 1998.

Hickey, M.P., Walterscheid, R.L., Schubert, G. Gravity wave heating and cooling in Jupiter's thermosphere. Icarus 148, 266–281, doi:10.1006/icar.2000.6472, 2000.

Hickey, M.P., Huang, T.-Y., Walterscheid, R. Gravity wave packet effects on chemical exothermic heating in the mesopause region. J. Geophys. Res. 108 (A12), 1448, doi:10.1029/2002JA009363, 2003.

Hines, C.O. Internal atmospheric gravity waves at ionospheric heights. Can. J. Phys. 38, 1441–1481, 1960.

Hines, C.O., Reddy, C.A. On the propagation of atmospheric gravity waves through regions of wind shear. J. Geophys. Res. 72, 1015–1034, 1967.

Hocking, W.K. Turbulence in the region 80–120 km. Adv. Space Res. 7 (10), 171–181, 1987.

Hocking, W.K. Two years of continuous measurements of turbulence parameters in the upper mesosphere and lower thermosphere made with a 2-MHz radar. J. Geophys. Res. 93, 2475–2491, 1988.

Hodges Jr., R.R. Generation of turbulence in the upper atmosphere by internal gravity waves. J. Geophys. Res. 72, 3455–3458, 1967.

Hodges Jr., R.R. Eddy diffusion coefficients due to instabilities in internal gravity waves. J. Geophys. Res. 74, 4087–4090, 1969.

Holton, J.R. The role of gravity wave induced drag and diffusion in the momentum budget of the mesosphere. J. Atmos. Sci. 39, 791–799, 1982.

Holton, J.R. The influence of gravity wave breaking on the general circulation of the middle atmosphere. J. Atmos. Sci. 40, 2497–2507, 1983.

Lindzen, R.S. Internal gravity waves in atmospheres with realistic dissipation and temperature. Part I: mathematical development and propagation of waves into the thermosphere. Geophys. Fluid Dyn. 1, 303–355, 1970.

Lindzen, R.S. Turbulence and stress owing to gravity wave and tidal breakdown. J. Geophys. Res. 86 (C10), 9707–9714, 1981.

此为试读,需要完整PDF请访问: www.ertongbook.com